Investigation of Aero-Elastic Effects on the DLR Results of the Fifth AIAA Drag Prediction Workshop

Stefan Keye[1] and Olaf Brodersen[2]
DLR, German Aerospace Center, 38108 Braunschweig, Germany

Melissa B. Rivers[3]
NASA Langley Research Center, Hampton, VA, 23681, USA

Static Fluid-Structure-Coupled (FSC) simulations were performed on NASA's Common Research Model (CRM) to assess the influence of aero-elastic effects on the numerical prediction of overall aerodynamic coefficients and wing static pressure distributions. Numerical results of both conventional Computational Fluid Dynamics (CFD) and coupled simulations were compared to experimental data from a wind tunnel test campaign in NASA's National Transonic Facility (NTF). Coupled analyses were performed using an in-house simulation procedure built around DLR's flow solver TAU and the commercial finite-element analysis code NASTRAN®. Results show a considerable reduction of deviations between computational results obtained during the 4th and 5th AIAA CFD Drag Prediction Workshops (DPW) and measured data when aero-elastic wing deformations are taken into account.

---

[1] Research Scientist, Dept. Transport Aircraft, Institute for Aerodynamics and Flow Technology, Lilienthalplatz 7.
[2] Head, Dept. Transport Aircraft, Institute for Aerodynamics and Flow Technology, Lilienthalplatz 7.
[3] Research Engineer, Configuration Aerodynamics Branch, Mail Stop 267, Senior Member AIAA.

Nomenclature

C_D = drag coefficient

C_L = lift coefficient

C_M = pitching moment coefficient

c = wing chord, m

c_p = pressure coefficient

F = force, N

H = altitude, m

i = CFD face centroid number

j = finite-element node number

M = moment of torsion, Nm

M_∞ = Mach number

r = radius, m

Re = Reynolds number

w = wing bending deflection, m

x = x coordinate, m

α = angle of incidence, degrees

ε = wing twist deflection, degrees

η = normalized spanwise coordinate

AMIF = Aerodynamic Mesh Interface Format

$C^2A^2S^2E$ = Center for Computer Applications in AeroSpace Science and Engineering

CRM = NASA Common Research Model

CSM = Computational Structural Mechanics

DLR = Deutsches Zentrum für Luft- und Raumfahrt e.V. (German Aerospace Center)

DPW = Drag Prediction Workshop

FSC = Fluid-Structure-Coupled simulation

$k\omega$-*SST* = two-equations Shear Stress Transport turbulence model

LU-SGS = Lower-Upper Symmetric Gauss-Seidel scheme

NTF = NASA National Transonic Facility

$RANS$ = Reynolds-averaged Navier-Stokes equations

RBF = Radial Basis Function

SA = Spalart-Allmaras turbulence model

$SSG/LLR\text{-}\omega$ = Reynolds-stress turbulence model

TWT = NASA Ames 11-Foot Transonic Wind Tunnel Facility

I. Introduction

THE accurate calculation of aerodynamic forces and moments is of significant importance during the design phase of an aircraft. Reynolds-averaged Navier-Stokes (RANS) equations based Computational Fluid Dynamics (CFD) has been strongly developed over the last two decades regarding robustness, efficiency, and the capability to handle aerodynamically complex configurations [1, 2]. Incremental aerodynamic coefficients of different transonic aircraft designs can be calculated with an acceptable reliability at the cruise design point and for non-separated flows. But regarding increments at off-design as well as absolute values significant challenges still exist to compute aerodynamic data and simulate the underlying flow physics with the accuracy and reliability required.

In addition to drag, pitching moments are difficult to predict because small deviations in the surface pressure distributions, e.g. due to neglecting wing bending and twist deformations caused by aerodynamic loads, can result in large discrepancies compared to experimental data. Flow separations that start to develop at off-design conditions, e.g. in corner-flows, at trailing edges, or shock-induced, can have a strong impact on the predictions of aerodynamic coefficients too.

Based on these challenges faced by the aircraft design CFD community, a working group of the AIAA Applied Aerodynamics Technical Committee initiated the CFD Drag Prediction Workshop (DPW) series in 2001, resulting in five international workshops to date. The participants and committee results are summarized in more than 120 papers [3–7]. The latest, fifth workshop took place in June 2012 in conjunction with the 30th AIAA Applied Aerodynamics Conference [8].

All workshops were focused on the following key objectives [6]:

- assess state-of-the-art CFD methods as practical aerodynamic tools for the accurate prediction

of forces and moments on industry-relevant aircraft configurations, with a focus on absolute as well as incremental values,

- setup an international forum of experts from industry, research and academia for the verification and validation of RANS based CFD methods by applying different meshing methods and turbulence models,
- define areas for additional research needed,
- build, use, and maintain a public-domain transonic flow database for transport aircraft geometries including CAD data, grids, and numerical and experimental results,
- document workshop findings and to disseminate through presentations and publications.

NASA and DLR's Institute of Aerodynamics and Flow Technology are supporting these objectives as committee members and participants [9–13].

The first three workshops used DLR transonic wind tunnel model configurations and experimental data achieved together with ONERA [3–5, 14, 15]. For the fourth and fifth workshops a new configuration designed for transonic flow conditions, the so-called Common Research Model (CRM), was defined by NASA and Boeing [16], see Fig. 1. In 2009 and 2010 wind tunnel test campaigns using the CRM were performed by NASA in the National Transonic Facility (NTF) at Langley Research Center and in the Ames 11-Foot Transonic Wind Tunnel (TWT). The data have been published recently in several papers and on the NASA CRM web site [17–20].

A major aspect came into focus when the DPW-4 and DPW-5 computational results of the participants were compared to the experimental data. Besides moderate discrepancies in drag at the cruise design point significant offsets of the pitching moments were observed. These were traced back to the model support system, which extends vertically from the aft fuselage, and to a deviation of spanwise wing twist distribution between the computational geometry and the manufactured wind tunnel model geometry [21, 22].

DLR results in DPW-4 and DPW-5 also showed differences between experimental data and numerical calculations of the wing pressure distributions, especially for the most outboard sections as presented in Figs. 2 and 3, which were found to be nearly independent of grid refinement level

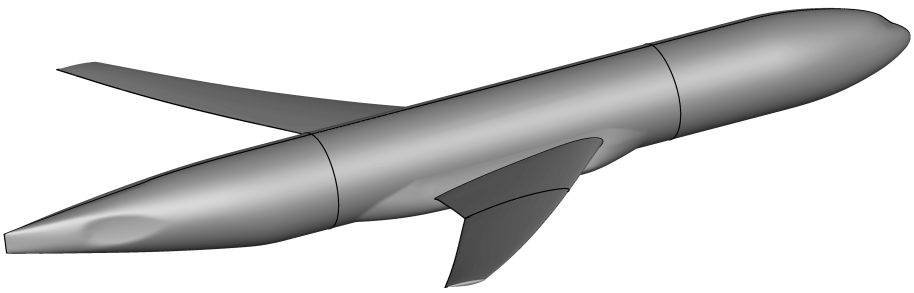

Fig. 1 NASA Common Research Model (CRM) without engines and horizontal tail plane.

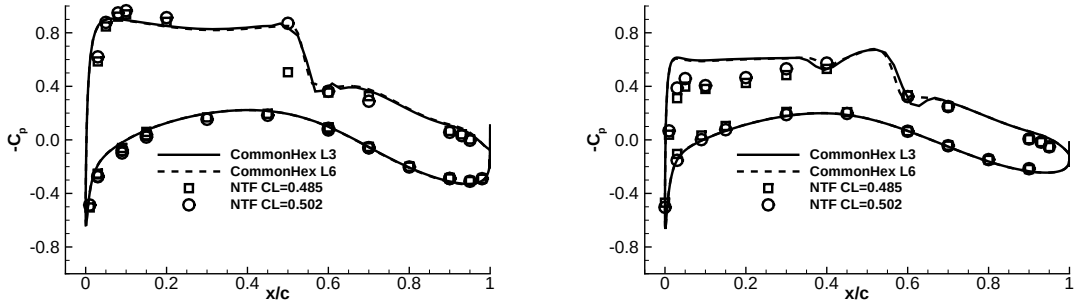

(a) $\eta = 0.501$ (b) $\eta = 0.95$

Fig. 2 Pressure distributions, TAU results for common grids (L2: coarse, L6: ultra fine), SA turbulence model, NASA NTF test data, $M_\infty = 0.85$, $Re = 5{\cdot}10^6$, $C_L = 0.5$.

(L3: medium, L6: ultra fine). Therefore, it is the objective of these investigations to evaluate the influence of static aero-elastic wing deformations onto pressure distributions and overall aerodynamic coefficients. NASA and DLR decided to perform, in addition to their other DPW investigations, fluid-structure-coupled simulations based on NASA's finite-element structural model of the CRM wind tunnel model and the DLR CFD solver TAU.

II. NASA Common Research Model and DPW-5 Test Cases

For DPW-5 the NASA Common Research Model (CRM) civil transport aircraft configuration for cruise flight conditions ($M_\infty = 0.85$, $C_L = 0.5$, altitude $H = 11,300m$) is used as the reference geometry. The CRM optionally has a horizontal stabilizer as well as engines and pylons. In DPW-5 only the wing-body configuration shown in Fig. 1 is used. The CRM was designed by NASA's Subsonic Fixed Wing Technical Working Group and by Vassberg et al. [16]. The wing has a slightly

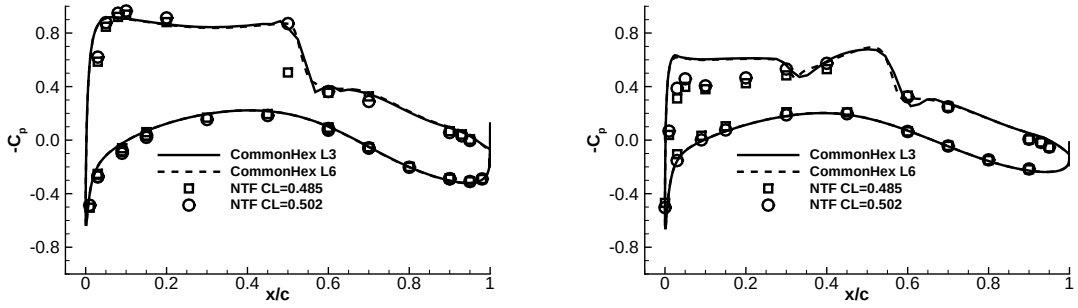

(a) η=0.501 (b) η=0.95

Fig. 3 Pressure distributions, TAU results for common grids (L2: coarse, L6: ultra fine), Menter kω-SST turbulence model, NASA NTF test data, $M_\infty = 0.85$, $Re = 5{\cdot}10^6$, $C_L = 0.5$.

Table 1 CRM wing geometrical data

Parameter	Value
Reference Area	$0.2797m^2$ [$3.007ft^2$]
Span	$1.587m$ [$62.46in$]
Mean Aerodynamic Chord	$0.1891m$ [$7.445in$]
Aspect Ratio	9.0
Taper Ratio	0.275
Sweep Angle at 1/4 Chord	35.0°

stronger pressure recovery at the last 10-15% local chord on the upper surface of the outboard wing section. The objective of this feature is to reduce boundary layer strength to control the development of a trailing edge separation and to create a challenge for turbulence models. The main geometrical features of the CRM are listed in Table 1. Further details are published by Vassberg [16]. The geometrical and experimental data of the model are published on the NASA CRM web site [20].

DPW-5 required two mandatory test cases as a minimum. Additional parameter, grid, and turbulence model variations were allowed.

Case 2, Buffet Study:

- Flow conditions: M_∞=0.85, Re=$5{\cdot}10^6$, steady flow simulations,
- α=[2.5°, 2.75°, 3.0°, 3.25°, 3.5°, 3.75°, 4.0°],

- Grids: medium (L3) common grid, custom grid.

III. Numerical Methods

A. CFD Solver

Since the mid 1990s the Reynolds-averaged Navier-Stokes solver TAU is under development at DLR. It can be traced back to the German CFD project MEGAFLOW which integrated developments of DLR, aircraft industry, and universities [23–25]. Today the software package is under continuous development by the institute's $C^2A^2S^2E$ department (Center for Computer Applications in AeroSpace Science and Engineering) and it is applied by DLR and European partners in industry and academia.

TAU is an edge-based, unstructured solver using the dual grid technique and fully exploits the advantages of hybrid grids. Turbulence models of different fidelities are available, e.g. the one-equation Spalart-Allmaras (SA), the two-equations Menter kω-SST, and the SSG/LLR-ω Reynolds-Stress model [26–28]. The numerical scheme is based on the Finite-Volume method and provides different spatial discretization schemes like central and upwind [25]. Here, a central scheme of second order accuracy, using the Jameson-type of artificial dissipation in scalar and matrix mode, has been applied [29, 30]. Time integration has been performed using both, the explicit Runge-Kutta multistage and the Lower-Upper Symmetric Gauss-Seidel (LU-SGS) schemes. TAU has been developed with a particular focus on industrial aeronautical applications, thus providing techniques like overlapping grids for treating unsteady phenomena and complex geometries. Further details of TAU can be found in Ref. [25].

B. Finite-Element Analysis

The computational structural mechanics (CSM) analysis code NASTRAN® [31] was originally developed for NASA in the late 1960s as a tool for designing more efficient space vehicles such as the Space Shuttle. The code has continuously evolved over the years with each new version providing enhancements with respect to analysis capabilities and numerical performance. After being released to the public NASTRAN® became widely used throughout the aerospace and automotive industries and in civil engineering applications and has become the industry standard in many fields

of application. Available analysis types include linear and non-linear static, modal, frequency and transient response, heat transfer, and design optimization.

C. Fluid-Structure-Coupled Simulation Procedure

DLR's steady state FSC simulation procedure, Fig. 4, incorporates the flow solver TAU and the commercial finite-element analysis software NASTRAN® as main components. Additional modules included are a bi-directional interpolation routine for mapping aerodynamic loads to the structural nodes and transferring structural deflections back to the CFD mesh, and a volume mesh deformation algorithm.

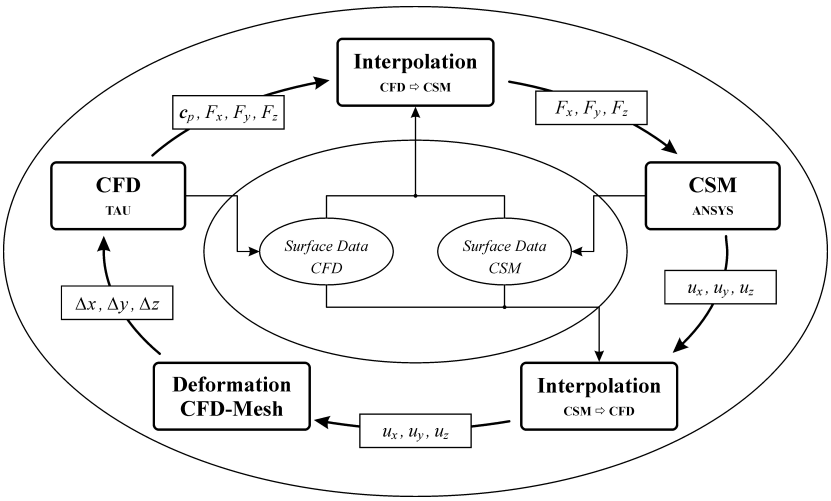

Fig. 4 Simulation procedure for Fluid-Structure-Coupled analyses.

The analysis starts from an initial RANS CFD solution, which is computed on the undeformed grid. Then, static pressure and friction coefficients along with the identifiers, coordinates, and connectivity of the grid nodes, which constitute the CFD coupling surface, are transferred to the interpolation module using the Aerodynamic Mesh Interface Format (AMIF) specification.

For each surface element in the CFD grid the interpolation module computes a force vector using pressure coefficient values, cell face area and cell orientation. Then, aerodynamic forces are mapped to the structural nodes located on the coupling surface. The corresponding finite-element surface data is provided from another AMIF file and processed in the same manner. Due to the considerable resolution difference, which usually exists between CFD and structural meshes, or when,

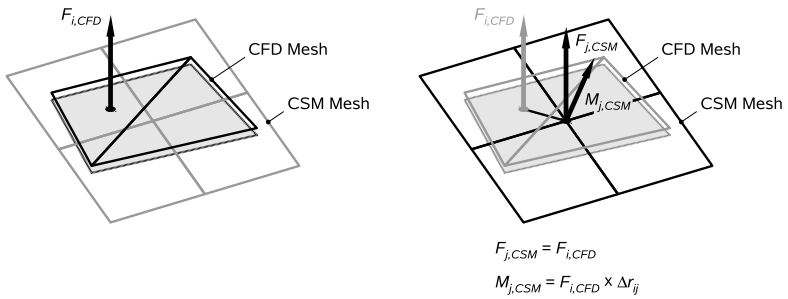

Fig. 5 Force mapping between CFD and CSM meshes.

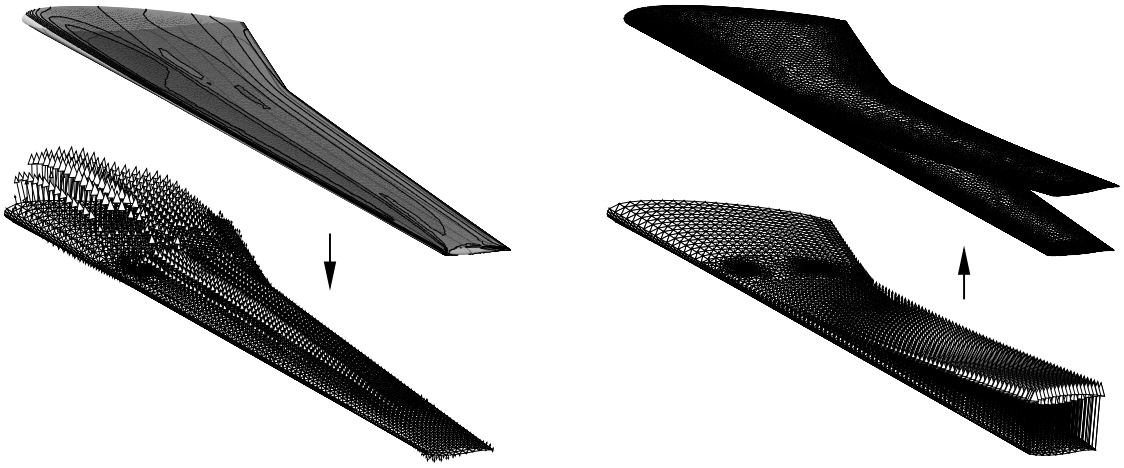

(a) Interpolation of static surface pressure (top) to nodal forces (bottom)

(b) Interpolation of structural deflections (bottom) to CFD surface mesh (top)

Fig. 6 Interpolation of aerodynamic loads and structural deflections.

as in this case, connectivity data of the finite-element surface nodes is not available, the application of a simple linear interpolation strategy is not applicable and a nearest neighbor search algorithm is used instead [32]. An assessment of both interpolation methods with respect to the coupling of aerodynamic forces between CFD and structural meshes is provided in Ref. [33]. For a given CFD face centroid i the nearest neighboring CSM grid point j is identified and a force component $F_{j,CSM}$ and associated moment $M_{j,CSM} = F_{i,CFD} \times \Delta r_{ij}$ are mapped to node j, Fig. 5. This procedure ensures a conservative interpolation with respect to both force and moment balance on CFD and CSM side. An example showing a computed c_p-distribution and the equivalent structural force distribution is given in Fig. 6 (a).

Next, nodal loads from the interpolation routine are re-formatted into NASTRAN® force cards

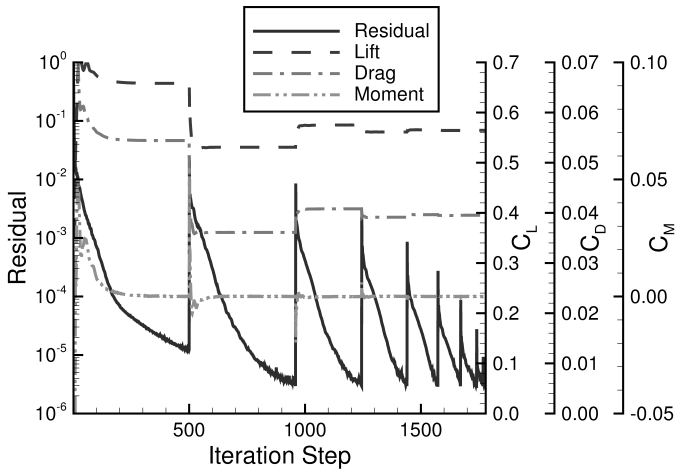

Fig. 7 Coupled simulation convergence history.

and linked to the bulk data file. A linear, static structural analysis is performed and the resulting nodal deflection components along the coupling surface are mapped back to the CFD surface mesh, Fig. 6 (b). Because the nearest neighbor search algorithm used before is not appropriate for deformation fields, an interpolation scheme based on radial basis functions (RBF) is used [32]. The technique is particularly well suited for smooth functions [34, 35], like the deformations of aerodynamic structures considered in this application.

Before a new flow solution is started, the interpolated surface nodal deflections are extrapolated into the volume mesh. This is achieved by applying the RBF interpolation functions used for the surface mesh deformation to the volume mesh nodes also. Additionally, the resulting deflections are superimposed with a weighting function based on wall distance in order to achieve a gradual decline of nodal deflections from the coupling surface into the flow field and to let them vanish for a specified distance, for example along the farfield boundaries. The method is applicable to both hybrid unstructured and block-structured meshes.

Finally, a new CFD solution is computed on the deformed mesh. A typical convergence history for a fluid-structure-coupled simulation is plotted in Fig. 7. The individual coupling steps are easily identified by steep increases in density residual and altered lift, drag, and pitching moment coefficient values. Iteration proceeds until user-defined convergence criteria, based on either flow or structural parameters, are accomplished.

DLR's fluid-structure-coupled simulation approach has been validated using a variety of test cases and flow conditions, including both wind tunnel [36] and flight test data [37].

IV. Computational Grids

A. CFD Grid

A six level common grids family of point-matched O-O topology multi-block grids has been build by Boeing [38]. The sequence is based on an extra-fine grid (L5) with $40.9 \cdot 10^6$ hexahedral elements. To limit grid sizes a 2-to-3 cell grid generation strategy was applied. The L6 grid (ultra fine) has been generated by refining L5 by a factor of 1.5 in each parameter direction. The coarser grids L4-L2 and L3-L1 have been defined by dividing L5 and L6 by 8, making them appropriate for multigrid [38]. The derived medium grid (L3) with $5.1 \cdot 10^6$ elements, Fig. 8, represents a common current grid size in industry for wing-fuselage configurations and will be used for the fluid-structure-coupled calculations.

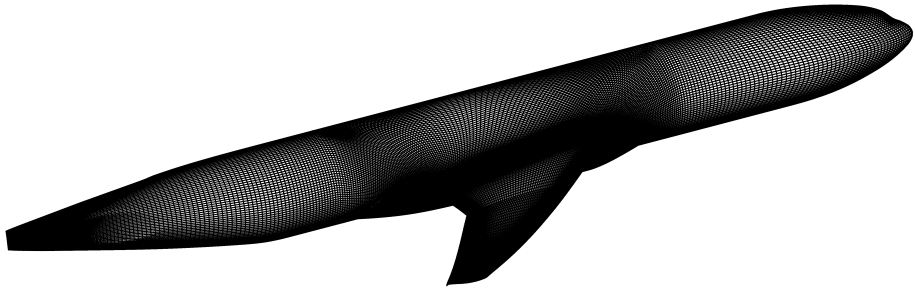

Fig. 8 Common hexahedral medium grid (L3) of DPW-5.

B. CSM Model

A NASTRAN® solid 4-node tetrahedral finite-element structural model of wing, fuselage, horizontal tail plane, engine nacelles, and balance interface was kindly made available by NASA Langley's Configuration Aerodynamics Branch, Fig. 9. The model includes both right and left sides to account for the wind tunnel model's non-symmetric inner structure. Joints between individual components are modeled with rigid body elements. A rigid suspension is assumed at the balance interference. The finite-element discretization consists of approximately $1.4 \cdot 10^6$ nodes, $6.8 \cdot 10^6$ elements, and $8.2 \cdot 10^6$ degrees-of-freedom. Bush elements were used to attach individual model com-

ponents to each other so that the user can remove and substitute components as needed. A variety of quality assurance checks were performed using MSC PATRAN® [39] 2011 and NASTRAN® 2010 to verify the CRM finite-element model. These checks included free-free model, 1-g static/equilibrium, strain-energy, element quality, element normal, element free-edge, coincident nodes, grid point singularities, round-off error, and grounding.

For the coupled simulations the engine nacelles and pylons were removed to more accurately represent the actual wind tunnel configuration. Coupling of aerodynamic loads between CFD simulation and finite-element analysis is established on the wing upper and lower surfaces.

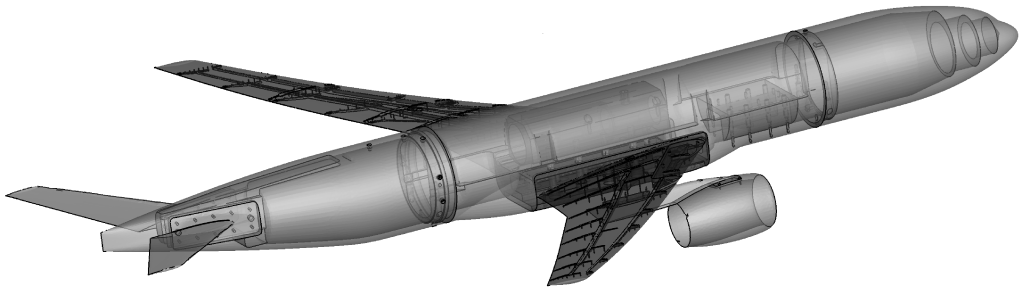

Fig. 9 CRM finite-element model.

V. Results

The purpose of the fluid-structure-coupled simulations was to determine the static aero-elastic equilibrium state for one selected DPW-5 test case and to assess the influence of wing deformations on static pressure distributions and overall aerodynamic coefficients, in particular pitching moment. The results shall help to quantify the effects, which have caused the observed deviations between CFD simulations and experiments.

FSC simulations were run for DPW-5 test case 2 (cf. Chapter II) flow conditions using the medium (L3) common grid and SA turbulence model. For an improved evaluation along with results obtained during recent investigations of support system effects [21, 22], the angle-of-attack is varied between $\alpha = 0.0°$ and $\alpha = 4.5°$ in steps of $\Delta\alpha = 0.5°$.

A. Overall Aerodynamic Coefficients

Generally, the aero-elastic effects observed on the CRM were found to be larger than for the DLR-F6 wing-body configuration [36] used during the Second and Third Drag Prediction Workshops. In Fig. 10, the overall aerodynamic coefficients C_L and C_D obtained from the conventional CFD and FSC simulations, respectively, together with experimental data from the NTF wind tunnel test campaign (Test 197, Run 44), are plotted as a function of angle-of-attack. The coupled simulation results show lower overall lift compared to the conventional CFD results, with the difference between FSC and CFD increasing with angle-of-attack. The lift reduction is due to the nose-down wing twist deformation induced by the geometric bending-torsion-coupling of the backward-swept wing as the wing is bent upwards by the external aerodynamic loads.

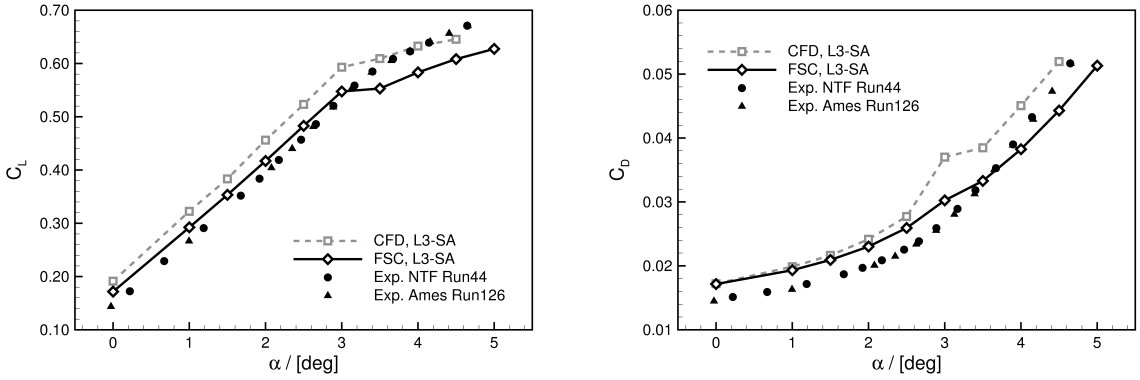

(a) Lift

(b) Drag

Fig. 10 Overall aerodynamic lift and drag coefficients for DPW-5 test case 2.

The drop in lift starting between $\alpha = 3.0°$ and $\alpha = 3.5°$ found only in the numerical data is due to an over-prediction of the side-of-body flow separation size in the medium (L3) hexahedral grid when using the SA turbulence model. The separation effect and related numerical issues are investigated and discussed in Ref. [40]. In the linear region, i.e. for $\alpha \leq 3.0°$, deviations between the coupled simulation results and experimental data are considerably smaller than for the conventional CFD analysis, Table 2. The remaining error is very similar to the differences found by Rivers et al. [21, 22] to be caused by the model support system. This suggests that including both aero-elastic and support system effects in the numerical simulation, together with a physically correct turbulence model, will allow for removing most of the previously observed deviations.

Table 2 Lift coefficient deviations of numerical predictions w.r.t. experimental results

Angle of Attack, degrees	Lift Coefficient Deviation	
	CFD	FSC
0.0	+0.0456	+0.0260
3.0	+0.0574	+0.0118

Differences in drag coefficient between conventional CFD and FSC remain very small for incidence angles up to 2.5°. The deviation at off-design conditions is caused by the shock-induced flow separation on the outboard wing. In the coupled simulation, the separation sets in later, i.e. at a higher angle-of-attack, and, compared to the conventional CFD analysis, extends over a smaller spanwise portion of the outboard wing, which is due to the lower local angles-of-attack in the outer region of the deformed wing.

For pitching moment coefficients, Fig. 11, the deviations between numerical and experimental data are greatly reduced by taking into account wing deformation in the coupled simulation. Still, considerable differences remain, even around the design point. Again, including support system effects appears likely to move the numerical predictions closer to the experimental data.

B. Static Pressure Distributions

Figure 12 shows a comparison of chordwise static pressure distributions between CFD and FSC simulations and wind tunnel test data taken from the NTF campaign for four different spanwise wing sections at $\alpha = 3.0°$. At the innermost section, Fig. 12 (a), where wing deformation is very

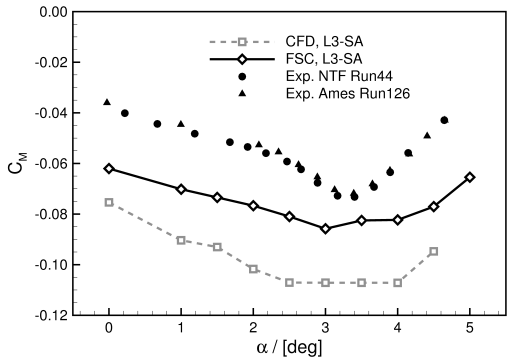

Fig. 11 Pitching moment coefficient for DPW-5 test case 2.

small, cf. Fig. 13 (b), both numerical methods are in good agreement with each other and the measured pressure distribution. Although twist deformation in this section is only $\varepsilon = -0.0115°$, the shock location predicted by the FSC simulation lies somewhat closer to the wind tunnel data. The mid-wing section, Fig. 12 (b), already shows some effects of aero-elastic deformation between the leading edge and about 75% chord, with a decreased rooftop pressure level, reduced pressure along most of the wing lower side, and, again, a more precise shock location. At $\eta = -0.727$, Fig. 12 (c), wing twist has increased to $\varepsilon = -1.09°$ and the differences between conventional CFD and FSC become even more apparent. Here, only the coupled simulation is in good agreement with both measured rooftop pressure levels and shock location. At the outermost section, Fig. 12 (d), the shock location as predicted by the FSC simulation has moved significantly downstream and a dual-shock pattern has developed. Twist deformation has increased to $\varepsilon = -1.41°$, considerably reducing

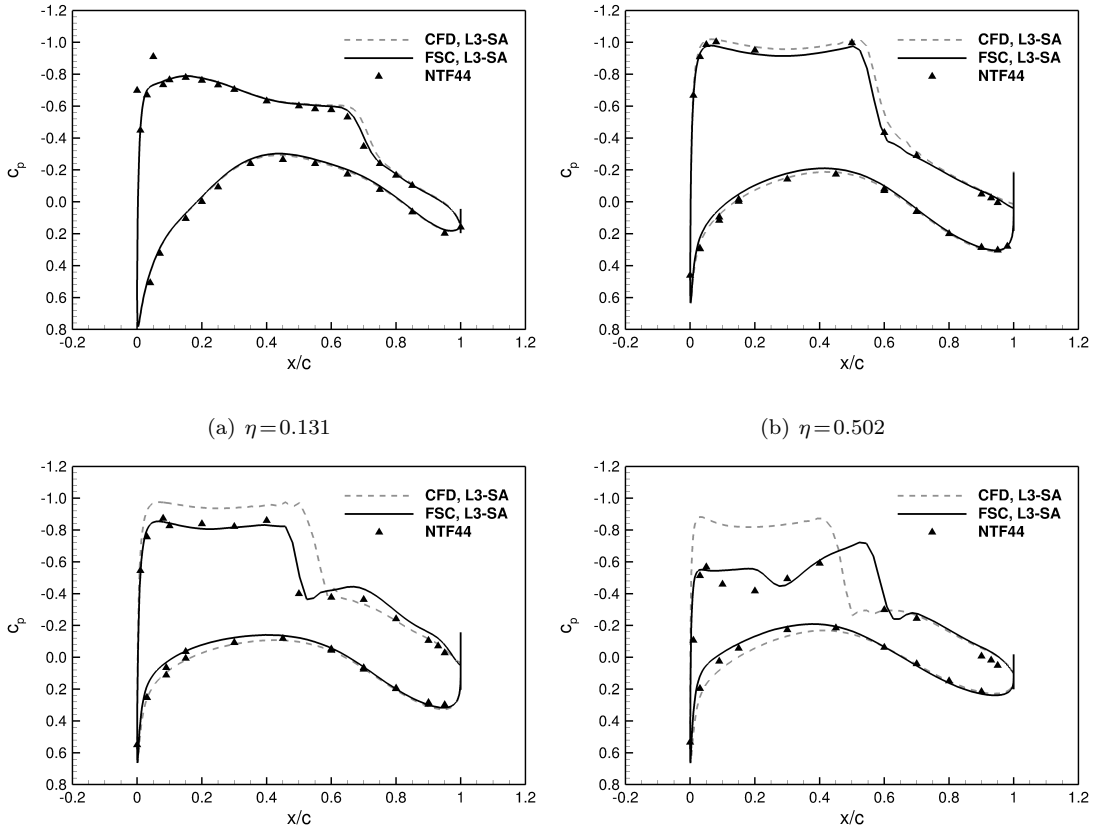

(a) $\eta = 0.131$

(b) $\eta = 0.502$

(c) $\eta = 0.727$

(d) $\eta = 0.950$

Fig. 12 Chordwise static pressure distribution at $\alpha = 3.0°$ for different spanwise wing sections; TAU only, Fluid-Structure-Coupled, and NASA NTF experiments.

the local incidence angle. As a result, the pressure distribution at $\eta = -0.950$ resembles those for conventional CFD computations at lower angles-of-attack, cf. Figs. 2 (b) and 3 (b), where a similar dual-shock system exists. Unfortunately, the true shock position can not be determined from the experimental data due to the limited spatial resolution of pressure taps in this section.

C. Wing Deformations

In Fig. 13 the wing bending and twist deformations with respect to the $c/4$-line are plotted as a function of angle-of-attack at wing tip (a) and as spanwise distribution for $\alpha = 3.0°$ (b). As previously seen with lift coefficient, Fig. 10 (a), good linearity exists for $\alpha \leq 3.0°$. Between $\alpha = 3.0°$ and $\alpha = 3.5°$ the onset of the side-of-body flow separation can be identified by small decreases in both bending and twist deformations. The declining slope for $\alpha > 3.0°$ is caused by the growing shock-induced flow separation on the outer wing.

The spanwise wing twist and bending distribution for $\alpha = 3.0°$ is plotted in Fig. 13 (b). Due to the fact that from $\eta \approx 0.40$ outward the $c/4$-line lies behind the model reference center, any aero-elastic wing deformation will not only result in a change of spanwise lift distribution, but also reduce the overall nose-down pitching moment (cf. Fig. 11).

Unfortunately, no experimental deformation data was available for comparison as the corresponding wind tunnel test was still ongoing at the time of publication of this paper.

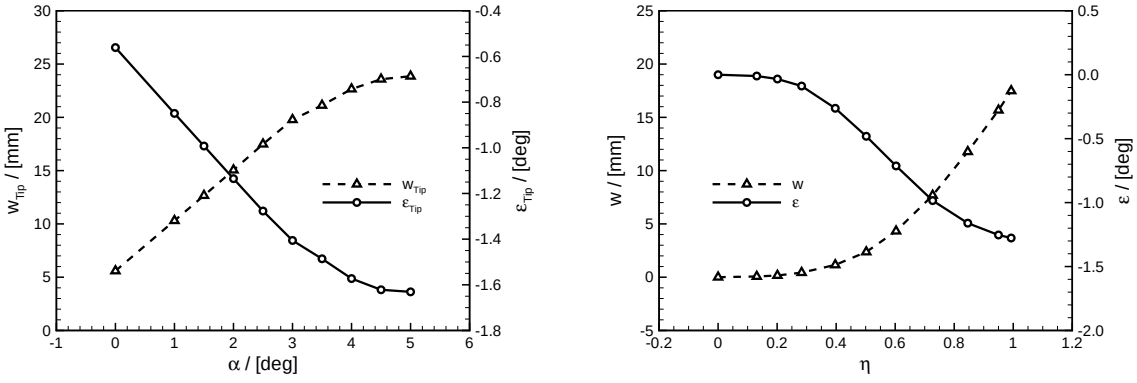

(a) Wing tip deformation vs. angle-of-attack

(b) Spanwise wing deformation

Fig. 13 Wing bending and twist deformations.

VI. Conclusions

The influence of wing deformations on static pressure distributions and overall aerodynamic coefficients of NASA's Common Research Model were investigated using the medium (L3) common grid, the Spalart-Allmaras turbulence model, and a finite-element structural model provided by NASA Langley. Static fluid-structure-coupled simulations were run at $M_\infty = 0.85$ and $Re = 5 \cdot 10^6$ with the angle-of-attack varying between $\alpha = 0.0°$ and $\alpha = 4.5°$. Numerical results were compared to experimental data from a wind tunnel test campaign in NASA's National Transonic Facility. Generally, the deviations of lift, drag, and pitching moment coefficients observed between DPW-4 and DPW-5 computational results and measured data are considerably reduced by taking into account elastic wing deformations. Lift coefficient values predicted by the coupled simulation are lower than for the conventional CFD computations, leading to considerably smaller deviations from the experimental data. For drag coefficients, significant differences between the conventional CFD and FSC analyses only occur at off-design flow conditions and are mostly due to variations in the development of the shock-induced separation on the outboard wing. Deviations between numerical and experimental pitching moment coefficients are substantially reduced by taking into account wing deformation. Due to the pitching moment's strong sensitivity with respect to the overall static pressure distribution, differences remain relatively large. Regarding chordwise static pressure distributions, some minor aero-elastic effects become visible in the mid-wing section, increasing in magnitude towards the wing tip. In general, the FSC simulations provide a significantly more accurate prediction of rooftop pressure levels, pressure distribution on the wing lower side, and shock location. Wing bending and twist deformations show a good linearity for $\alpha \leq 3.0°$. For higher angles-of-attack, wing deformations are influenced by the side-of-body flow separation and the shock-induced separation on the outer wing.

Based on the results found in this study and by Rivers et al. [21, 22], it is suggested that further numerical investigations should include both aero-elastic and support system effects, together with a high-quality turbulence model, which takes into account normal stress anisotropy.

Acknowledgments

The authors would like to thank the current AIAA DPW Committee members, namely (in alphabetical order of their organisations): J. Vassberg, E. Tinoco, M. Mani and B. Rider (Boeing), D. Levy, K. Laflin and T. Zickuhr (Cessna), M. Murayama (JAXA), R. Wahls and J. Morrison (NASA), and D. Mavriplis (University of Wyoming) for the excellent collaboration.

References

[1] Becker, K. and Vassberg, J., "Numerical Aerodynamics in Transport Aircraft Design," *Notes on Numerical Fluid Mechanics and Multidisciplinary Design*, edited by E.-H. Hirschel and E. Krause, Vol. 100, Springer, 2009, pp. 209–220.

[2] Rossow, C.-C. and Cambier, L., "European Numerical Aerodynamics Simulation Systems," *Notes on Numerical Fluid Mechanics and Multidisciplinary Design*, edited by E.-H. Hirschel and E. Krause, Vol. 100, Springer, 2009, pp. 189–208.

[3] Levy, D., Zickuhr, T., Vassberg, J., Agrawal, S., Wahls, R., Pirzadeh, S., and Hemsch, M., "Summary of Data from the First AIAA CFD Drag Prediction Workshop," AIAA Paper 2002–0841, Jan. 2002.

[4] Laflin, K., Klausmeyer, S., Zickuhr, T., Vassberg, J., Wahls, R., Morrison, J., Brodersen, O., Rakowitz, M., Tinoco, E., and Godard, J.-L., "Data Summary from Second AIAA Computational Fluid Dynamics Drag Prediction Workshop." *AIAA Journal of Aircraft*, Vol. 42, No. 5, 2005, pp. 1165–1178.

[5] Vassberg, J., Tinoco, E., Mani, M., Brodersen, O., Eisfeld, B., Wahls, R., Morrison, J., Zickuhr, T., Laflin, K., and Mavriplis, D., "Abridged Summary of the Third AIAA Computational Fluid Dynamics Drag Prediction Workshop," *AIAA Journal of Aircraft*, Vol. 45, No. 3, pp. 781-798, 2008.

[6] Vassberg, J., Tinoco, E., Mani, M., Zickuhr, T., Levy, D., Brodersen, O., Crippa, S., Wahls, R., Morrison, J., Mavriplis, D., and Murayama, M., "Summary of the Fourth AIAA Drag Prediction Workshop." Paper 2010–4547, AIAA, June 2010.

[7] Levy, D., Laflin, K., Tinoco, E., Vassberg, J., Mani, M., Rider, B., Rumsey, C., Wahls, R., Morrison, J., Brodersen, O., Crippa, S., Mavriplis, D., and Murayama, M., "Summary of Data from the Fifth AIAA CFD Drag Prediction Workshop," AIAA Paper to be published, Jan. 2013.

[8] AIAA, "Drag Prediction Workshop," [online database], http://aaac.larc.nasa.gov/tsab/cfdlarc/aiaa-dpw, 2013.

[9] Rakowitz, M., Sutcliffe, M., Eisfeld, B., Schwamborn, D., Bleeke, H., and Fassbender, J., "Structured and Unstructured Computations on the DLR–F4 Wing–Body Configuration," Paper 2002-0837, AIAA,

2002.

[10] Brodersen, O., Rakowitz, M., Amant, S., Larrieu, P., Destarac, D., and Sutcliffe, M., "Airbus, ONERA, and DLR Results from the Second AIAA Drag Prediction Workshop." *AIAA Journal of Aircraft*, Vol. 42, No. 4, pp. 932–940, 2005.

[11] Brodersen, O., Eisfeld, B., Raddatz, J., and Frohnapfel, P., "DLR Results from the Third AIAA CFD Drag Prediction Workshop." *AIAA Journal of Aircraft*, Vol. 45, No. 3, pp. 823–836, 2008.

[12] Brodersen, O., Crippa, S., Eisfeld, B., Keye, S., and Geisbauer, S., "DLR Results from the Fourth AIAA CFD Drag Prediction Workshop," AIAA Paper 2010–4223, June 2010.

[13] Brodersen, O. and Crippa, S., "RANS-based Aerodynamic Drag and Pitching Moment Predictions for the Common Research Model." *to be publsihed*, DGLR STAB Workshop 2012.

[14] Rossow, C.-C., Godard, J., Hoheisel, H., and Schmitt, V., "Investigation of Propulsion Integration Interference on a Transport Aircraft Configuration," AIAA Paper 92–3097, June 1992.

[15] Rudnik, R., Sitzmann, M., Godard, J.-L., and Lebrun, F., "Experimental Investigation of the Wing-Body Juncture Flow on the DLR-F6 Configuration in the ONERA S2MA Facility," Paper 2009–4113, AIAA, 2009.

[16] Vassberg, J., DeHaan, M., Rivers, S., and Wahls, R., "Development of a Common Research Model for Applied CFD Validation Studies," Paper 2008–6919, AIAA, June 2008.

[17] Rivers, M., "Experimental Investigations on the NASA Common Research Model," Paper 2010–4218, AIAA, June 2010.

[18] Rivers, M. and Dittberner, A., "Experimental Investigations of the NASA Common Research Model in the NASA Langley National Transonic Facility and NASA Ames 11-Ft Transonic Wind Tunnel," Paper 2011–1126, AIAA, January 2011.

[19] Zilliac, G., Pulliam, T., Rivers, M., Zerr, J., Delgado, M., Halcomb, N., and Lee, H., "A Comparison of the Measured and Computed Skin Friction Distribution on the Common Research Model," Paper 2011–1129, AIAA, January 2011.

[20] NASA, "Common Research Model," [online web site], http://commonresearchmodel.larc.nasa.gov/, 2012.

[21] Rivers, M. and Hunter, G., "Support System Effects on the NASA Common Research Model," Paper 2012–0707, AIAA, January 2012.

[22] Rivers, M., Hunter, G., and Campbell, R., "Further Investigation of the Support System Effects and Wing Twist on the NASA Common Research Model," Paper 2012–3209, AIAA, June 2012.

[23] Galle, M., "Ein Verfahren zur numerischen Simulation kompressibler, reibungsbehafteter Strömungen

auf hybriden Netzen," Phd thesis, Uni Stuttgart, 1999.

[24] Kroll, N., Rossow, C.-C., Becker, K., and Thiele, F., "MEGAFLOW – A Numerical Flow Simulation System," *Aerospace Science Technology*, Vol. 4, 2000, pp. 223–237.

[25] Gerhold, T., "Overview of the Hybrid RANS Code TAU," *MEGAFLOW*, edited by N. Kroll and J. Fassbender, Vol. 89 of *Notes on Numerical Fluid Mechanics and Multidisciplinary Design*, Springer, 2005, pp. 81–92.

[26] Spalart, P. and Allmaras, S., "A One–Equation Turbulence Model for Aerodynamic Flows," AIAA Paper 1992–0439, 1992.

[27] Menter, F. R., "Two-Equation Eddy-Viscosity Turbulence Models for Engineering Applications," *AIAA Journal*, Vol. 32, No. 8, 1994, pp. 1598–1605.

[28] Eisfeld, B. and Brodersen, O., "Advanced Turbulence Modelling and Stress Analysis for the DLR-F6 Configuration," Paper 2005–4727, AIAA, June 2005.

[29] Jameson, A., Schmidt, W., and Turkel, E., "Numerical Solution of the Euler Equations by Finite Volume Methods using Runge–Kutta Time Stepping Schemes," AIAA Paper 81–1259, Jan. 1981.

[30] Swanson, R. C. and Turkel, E., "On Central Differences and Upwind Schemes." *Journal of Computational Physics*, Vol. 101, pp., 1992.

[31] MSC Software Corporation, "Product Information," [online web site], https://www.mscsoftware.com/product/msc-nastran, 2013.

[32] Heinrich, R., Wild, J., Streit, T., and Nagel, B., "Steady Fluid-Structure Coupling for Transport Aircraft," ONERA-DLR Aerospace Symposium, Oct. 2006.

[33] Heinrich, R., Kroll, N., Neumann, J., and Nagel, B., "Fluid-Structure Coupling for Aerodynamic Analysis and Design - A DLR Perspective," AIAA Paper 2008-0561, Jan. 2008.

[34] Hounjet, M. and Meijer, J., "Evaluation of Elastomechanical and Aerodynamic Data Transfer Methods for Non-Planar Configurations in Computational Aeroelastic Analysis," Intern. forum on aeroelasticity and structural dynamics, manchester, uk, June 1995.

[35] Beckert, A. and Wendland, H., "Multivariante interpolation for fluid-structure interaction problems using radial basis functions," *Aerospace Science and Technology*, Vol. 5, No. 2, pp. 125–134, 2001.

[36] Keye, S. and Rudnik, R., "Aero-Elastic Simulation of DLR's F6 Transport Aircraft Configuration and Comparison to Experimental Data," Paper 2009–0580, AIAA, Jan. 2009.

[37] Keye, S., "Fluid-Structure Coupled Analysis of a Transport Aircraft and Flight-Test Validation," *AIAA Journal of Aircraft*, 2011, Vol. 48, No. 2, 2011, pp. 381–390.

[38] Vassberg, J., "A Unified Baseline Grid about the Common Research Model Wing-Body for the Fifth

AIAA CFD Drag Prediction Workshop." Paper 2011–3508, AIAA, June 2011.

[39] MSC Software Corporation, "Product Information," [online web site], https://www.mscsoftware.com/product/patran, 2013.

[40] Keye, S., Togiti, V., Eisfeld, B., Brodersen, O., and Rivers, M., "Investigation of Fluid-Structure-Coupling and Turbulence Model Effects on the DLR Results of the Fifth AIAA CFD Drag Prediction Workshop," AIAA Paper 2013–2509, AIAA, June 2013.